# The Role of the Indian Ocean in Controlling the Formation of Multiyear El Niños through Subtropical ENSO Dynamics

YONG-FU LIN[a] AND JIN-YI YU[a]

[a] *Department of Earth System Science, University of California, Irvine, California*

(Manuscript received 21 May 2023, in final form 13 October 2023, accepted 19 October 2023)

ABSTRACT: This study explores the key differences between single-year (SY) and multiyear (MY) El Niño properties and examines their relative importance in causing the diverse evolution of El Niño. Using a CESM1 simulation, observation/reanalysis data, and pacemaker coupled model experiments, the study suggests that the Indian Ocean plays a crucial role in distinguishing between the two types of El Niño evolution through subtropical ENSO dynamics. These dynamics can produce MY El Niño events if the climatological northeasterly trade winds are weakened or even reversed over the subtropical Pacific when El Niño peaks. However, El Niño and the positive Indian Ocean dipole (IOD) it typically induces both strengthen the climatological northeasterly trades, preventing the subtropical Pacific dynamics from producing MY events. MY events can occur if the El Niño fails to induce a positive IOD, which is more likely when the El Niño is weak or of the central Pacific type. Additionally, this study finds that such a weak correlation between El Niño and the IOD occurs during decades when the Atlantic multidecadal oscillation (AMO) is in its positive phase. Statistical analyses and pacemaker coupled model experiments confirm that the positive AMO phase increases the likelihood of these conditions, resulting in a higher frequency of MY El Niño events.

KEYWORDS: Climate; Indian Ocean; ENSO; Climate models

## 1. Introduction

Intensive research efforts have been recently made toward understanding the event-to-event differences in El Niño–Southern Oscillation (ENSO) properties (i.e., ENSO complexities), with particular focuses on their spatial patterns and temporal evolutions. The interest was motivated from noting that the central location of ENSO's sea surface temperature anomalies (SSTAs) has appeared to shift from the tropical eastern Pacific (EP) to the tropical central Pacific (CP) in recent decades (e.g., Ashok et al. 2007; Kao and Yu 2009; Capotondi et al. 2015). Previous studies further divide CP El Niño into two subtypes (Wang and Wang 2013; Wang et al. 2018), which gives more evidence for event-to-event differences in El Niño and ENSO complexities. While the observational data are still too short to conclude that the ENSO durations have also significantly changed, there have been indications that multiyear (MY) El Niño and La Niña events have occurred frequently recently. Beside the very recent "triple-dip" La Niña event that lasted from 2019 to March 2023, MY El Niño events have also occurred several times so far in the twenty-first century, including in the 2002–04, 2014–16, and the 2018–20 El Niños.

Traditional views consider that the fundamental dynamics of ENSO take place in the tropical Pacific (TP), with the subtropical Pacific (SP) playing a comparatively minor role. In the TP ENSO dynamic, the coupling of surface wind, SST, and thermocline variations along the equatorial Pacific is emphasized (e.g., Battisti and Hirst 1989; Jin 1997; Suarez and Schopf 1988). Earlier studies regarded subtropical Pacific processes as either part of stochastics forcing in the TP ENSO dynamics (e.g., Penland and Sardeshmukh 1995) or as precursors to trigger ENSO events through the TP ENSO dynamics (Chang et al. 1996). However, with the increasing recognition of the existence of the CP ENSO, the deterministic effect of subtropical Pacific processes on ENSO development has gained more emphasis (Kao and Yu 2009; Yu et al. 2010, 2011, 2012, 2017; Wang et al. 2019; Chen et al. 2019; Zheng et al. 2021; Fan et al. 2023). The physical processes underlying this deterministic effect are best described by the seasonal footprinting mechanism (Vimont et al. 2003). This mechanism elucidates how trade wind anomalies over the northeastern (NE) Pacific can induce subtropical Pacific SST anomalies, which in turn can be sustained and propagated to the tropical Pacific through the wind–evaporation–SST (WES) feedback (Xie and Philander 1994). Other studies have also suggested that subtropical trade wind anomalies can trigger the CP ENSO through upper oceanic circulations (Anderson 2004; Anderson et al. 2013; Wang et al. 2019; Guan et al. 2023).

This SP ENSO dynamic has recently been proposed as a significant contributor to the complex evolution patterns of ENSO by Yu and Fang (2018). They argued that the SP ENSO dynamic is more crucial than the TP ENSO dynamic in explaining why ENSO events can exhibit SY and MY patterns. The TP ENSO dynamic, centered on equatorial thermocline variations, tends to create a negative feedback to the ENSO SST variation, resulting in the succession of El Niño and La Niña and favoring SY ENSO events. In contrast, the SP ENSO dynamic permits an El Niño event to lead to another El Niño event in the following year, becoming an MY El Niño event, or to a La Niña event, becoming an SY event. The outcome depends on whether the El Niño event can trigger a warm or cold phase of the seasonal footprinting mechanism. Therefore, the SP ENSO dynamic can generate both

*Corresponding author*: Yong-Fu Lin, yongful@uci.edu

DOI: 10.1175/JCLI-D-23-0297.1

SY and MY ENSO events and serve as a crucial source of ENSO complexities.

Interbasin interactions between the Pacific and neighboring Atlantic or Indian Oceans (Horii and Hanawa 2004; Kug and Kang 2006; Okumura et al. 2011; Ham et al. 2013; Cai et al. 2019; Chen et al. 2019; Okumura 2019; Chikamoto et al. 2020; Kim and Yu 2022; Wu et al. 2019, 2021; Wang and Wang 2021; Hasan et al. 2022) also play a role in affecting the evolution pattern of ENSO. For example, during the developing fall [September$^0$–November$^0$ (SON$^0$)] of an El Niño event, a positive phase of the Indian Ocean dipole (IOD) is typically induced, followed by a positive Indian Ocean Basin (IOB) pattern during its peak winter to decay spring (December$^0$–May$^1$). These SST anomalies in the Indian Ocean can create an anomalous anticyclone in the northwest Pacific during the El Niño's decaying summer (June$^1$–August$^1$), which induces easterly anomalies over the equatorial western Pacific. The resulting wind anomalies can excite upwelled oceanic Kelvin waves propagating eastward, which accelerates El Niño's demise (Kug and Kang 2006; Izumo et al. 2010; Cai et al. 2019; Kim and Yu 2021). Through this TP ENSO dynamic, the Pacific–Indian Ocean interactions contribute to the formation of SY El Niño events.

In the recent study by Kim and Yu (2022), they explored how the characteristics of ENSO (specifically the location and intensity of ENSO SSTAs) influence the activation of TP ENSO dynamics, SP ENSO dynamics, or interbasin interactions, thereby impacting the SY or MY evolution of the ENSO event. However, their focus was solely on the SP ENSO dynamics triggered by extratropical atmospheric sea level pressure (SLP) disturbances associated with the North Pacific Oscillation (NPO). As detailed in Fang and Yu (2020), the key to initiating SP ENSO dynamics lies in the emergence of trade wind anomalies over the northeastern Pacific. These anomalies can arise not only from the NPO but also from various other processes, such as the influence of Indian Ocean SSTAs. In the present study, we consider all processes that could induce trade wind anomalies to activate SP ENSO dynamics and investigate how they can be affected by ENSO's properties. We also provide a quantification of the relative strengths of TP and SP ENSO in the formation of MY El Niño events. Additionally, we quantify the relative strengths of TP and SP ENSO in shaping the occurrence of MY El Niño events. To conduct this investigation, we utilized observational data spanning either 1854–2018 or 1948–2018, as well as a 2200-yr-long simulation generated by a coupled climate model. Further validation of our findings was achieved through experiments using coupled climate models.

## 2. Datasets and methods

### a. Datasets

This study utilized monthly SST data from the Extended Reconstructed Sea Surface Temperature (ERSST) version 5 provided by the National Centers for Environmental Information/National Oceanic and Atmospheric Administration (Huang et al. 2017). This dataset has a horizontal resolution of 2° × 2° and covers the time period from 1854 to the present day. Monthly atmospheric variables such as wind fields and SLP were obtained from the National Centers for Environmental Prediction–National Center for Atmospheric Research (NCEP–NCAR) reanalysis 1 (Kalnay et al. 1996), which has a horizontal resolution of 1.875° × 1.875° and is available from 1948 to the present. Anomalies were calculated by subtracting the monthly climatology, based on the respective analysis periods (either 1948–2018 or 1854–2018), after the removal of linear trends. The analysis period for the observational analysis is 1854–2018 if the analysis involves only oceanic variables but 1948–2018 if atmospheric variables are required.

### b. CESM1 preindustrial simulation

To address the issue of a limited number of ENSO events in the observational data, we expanded our analyses by including a 2200-yr preindustrial simulation produced by the Community Earth System Model, version 1 (CESM1; Kay et al. 2015). Our analysis focused on the model years 400–2200. Previous research has demonstrated that the CESM1 model is capable of reasonably reproducing observed ENSO characteristics, including reoccurrence frequencies, amplitude ranges, spatial structures, and temporal evolutions (e.g., DiNezio et al. 2017; Wu et al. 2019; Kim and Yu 2020). Additionally, previous studies have indicated that this CESM1 simulation accurately captures various contrasting features of SY and MY ENSO events as observed (e.g., Kim and Yu 2020, 2021, 2022; Zhu and Yu 2022). Anomalies of the model simulations were similarly calculated by subtracting the climatological values for each calendar month after the removal of linear trends.

### c. Classification of SY and MY El Niño events

In this particular study, seasons for the Northern Hemisphere were utilized. The El Niño year was designated as year 0, while the year following the El Niño decay was referred to as year 1, for all months on the calendar. The Climate Prediction Center criteria were followed to identify an El Niño event, which required the 3-month running mean Niño-3.4 index (i.e., SSTAs averaged in the region of 5°S–5°N, 170°–120°W) to have a value of 0.5°C or more. During the study period from 1854 to 2018, a total of 37 El Niño events were identified and documented in Table 1. For the CESM1 simulation, an El Niño event was recognized if its first winter (November$^0$–January$^1$) Niño-3.4 index exceeded 0.5 standard deviations (0.57°C). The CESM1 preindustrial simulation between model years 400 and 2200 identified a total of 352 El Niño events.

The classification of an El Niño as either an SY or MY event was determined by the Niño-3.4 index during its second winter. If the Niño-3.4 index was equal to or less than zero, the El Niño was categorized as an SY event; on the other hand, if the index was above zero, it was categorized as an MY event. As a result, our classification method identifies MY events that encompass not only cases where one El Niño event is succeeded by another El Niño event but also instances where a single El Niño event persists into the second year, albeit with its second-winter Niño 3.4 index dropping below 0.5 standard deviations. Since the objective of this study is to unveil the distinct physical processes responsible for determining whether El Niño–related warming in SSTAs can be sustained from the first to the

TABLE 1. SY and MY El Niño events during 1854–2018.

| Single-year events (1854–2018) | Multiyear events (1854–2018) |
|---|---|
| 1855/56, 1902/03, 1911/12, 1921/22, 1923/24, 1925/26, 1930/31, 1951/52, 1953/52, 1963/64, 1965/66, 1972/73, 1982/83, 1994/95, 1997/98, 2004/05, 2006/07, 2009/10 | 1857–59, 1876–78, 1880–82, 1884–86, 1887–89, 1895–97, 1899–01, 1904–06, 1913–15, 1918–20, 1940–42, 1957–58, 1968–70, 1976–78, 1979–81, 1986–88, 1991–93, 2002–04, 2014–16 |

second years, there is no inherent justification for these physical processes to require that the SSTA warming in the second year must persist above or equal a specific threshold (e.g., 0.5 standard deviations of the Niño-3.4 index). Therefore, our classification methods are reasonable for distinguishing El Niños into SY and MY events for analysis.

### d. Climate indices

In this study, five climate indices were utilized: the cold tongue index (CTI), zonal location (ZL) index of ENSO, the IOD index, the NPO index, and the Atlantic multidecadal oscillation (AMO) index. The CTI was calculated as the averaged SSTAs within the cold tongue region (6°N–6°S, 180°–90°W) and was used to represent the intensity of ENSO (Deser and Wallace 1990). A CTI value smaller (larger) than one standard deviation classified an El Niño event as weak (strong). The ZL index was utilized to determine whether the maximum center of an ENSO event was located more toward the tropical eastern or central Pacific and was calculated as the SSTA difference between a tropical eastern Pacific region (5°S–5°N and 160°–100°W) and a tropical central Pacific region (5°S–5°N and 150°E–160°W) in CESM1. A more positive (negative) value of the ZL index indicates that the ENSO event was located more toward the tropical eastern (central) Pacific (Kim and Yu 2022). For observations, the ZL index is defined as the SSTA difference in the Niño-3 region (5°S–5°N, 150°–90°W) and the Niño-4 region (5°S–5°N, 160°E–150°W). The IOD index was calculated as the normalized difference in SSTAs between the western Indian Ocean (10°S–10°N, 50°–70°E) and the southeastern Indian Ocean (0°–10°S, 90°–110°E) during the boreal fall, which is the season when IOD events typically peak (Saji et al. 1999). The NPO index represented a north–south seesaw mode of winter SLP variations over the North Pacific and was defined by the principal component corresponding to the second empirical orthogonal function (EOF) mode of normalized SLP anomalies over the North Pacific (20°–60°N, 120°E–80°W) during winter (Rogers 1981). Last, the AMO index was obtained from NOAA's Physical Sciences Division and was defined as the detrended average of SSTAs over the North Atlantic from the equator to 70°N (Enfield et al. 2001).

### e. Strengths of the TP and SP ENSO dynamics

We also define TP and SP indices to quantify the strength of the TP and SP ENSO dynamics during El Niño events. These two indices were calculated by applying a multivariable EOF (MEOF) analysis to combined anomalies of surface wind, SST, and sea surface height (SSH). Following the approach of Yu and Fang (2018), the analysis was performed using a two-step procedure. First, a spatial EOF analysis was separately applied to the SST, wind, and SSH anomalies to obtain their individual leading spatial EOF modes. Second, a temporal EOF analysis was applied to the combined principal components (PCs) of the leading spatial EOF modes of each variable to obtain the leading coupled modes among the variables. The first three MEOFs yield the leading coupled modes associated with ENSO, with one being related to the ENSO mature mode (as the MEOF1 mode) and the others being the SP and TP ENSO dynamic modes (as the MEOF2 and MEOF3 modes). These three MEOF modes resemble the classical spatiotemporal patterns associated with the three MEOF modes in Yu and Fang (2018; see their Fig. 1). The PCs of MEOF2 and MEOF3 were defined as the SP and TP indices in this study, respectively.

### f. The coupled AGCM–SOM pacemaker experiments

A coupled model consisting of an atmospheric general circulation model (AGCM) and a mixed layer slab ocean model (SOM) was utilized in the experiments. The AGCM used in the experiments was NCAR's Community Atmospheric Model, version 3.0 (CAM3.0), which had a T42 Eulerian spectral resolution and 26 vertical levels. The experiments conducted were an AMO-positive experiment and an AMO-negative experiment. The AGCM was forced by prescribing North Atlantic (0°–70°N) SSTs related to the positive and negative phases of the AMO, while the SOM determined SSTs elsewhere. To determine the SSTAs of the AMO, North Atlantic SSTAs were regressed onto the AMO index using 1900–2015 observations. The regressed SSTAs were then added to or subtracted from the observed SST climatology to prescribe the North Atlantic SSTs in the AMO-positive or AMO-negative experiment. The experiments were integrated for 120 years, with the model output from the last 100 years analyzed [see Lyu et al. (2017) for details].

### g. The fully coupled CESM1 pacemaker experiments

The study's conducted experiments employed the CEMS1.2.2 framework (for detailed information, refer to https://www.cesm.ucar.edu/models/cesm1.2/). These experiments utilized the B1850C5CN compset of CESM1.2.2, operating in a fully coupled mode, with the f19_g16 model configuration. This configuration featured a horizontal resolution of about 2° and 30 vertical levels vertically in the Community Atmospheric Model version 5.3 (CAM5.3). Additionally, the Parallel Ocean Program version 2 (POP2) had a horizontal resolution of approximately 1° and 60 vertical levels.

The experimentation encompassed an AMO-positive experiment and an AMO-negative experiment (Y.-F. Lin et al. 2023). In the pacemaker experiments, the North Atlantic region (0°–70°N) SSTs were adjusted to the model's climatology, incorporating the observed AMO-positive or AMO-negative

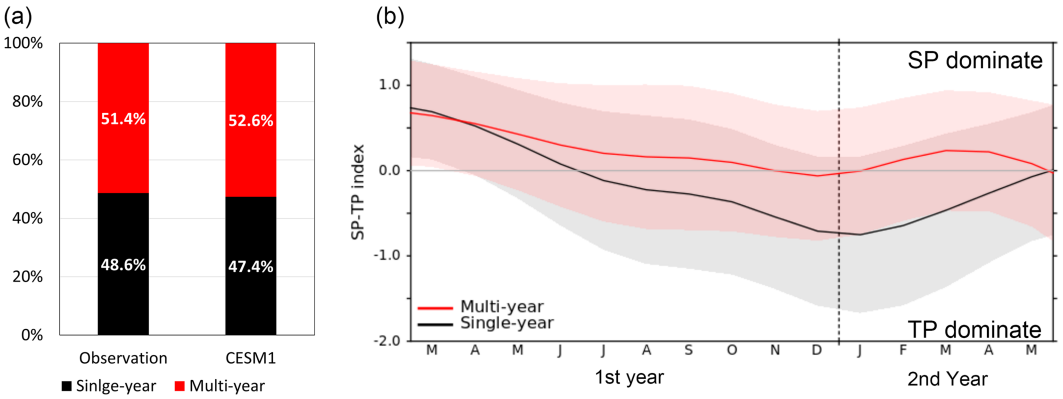


FIG. 1. (a) The relative percentages of SY (black bars) and MY (red bars) El Niño events in the observations from 1854 to 2018 and the preindustrial CESM1 model simulation during the model coverage years 400–2200. (b) The difference between the TP and SP indices composite SY (black line) and MY (red line) El Niño events in CESM1. Shadings denote one standard deviation. The black dashed line indicates the dividing line between the first year and the second year.

SST pattern. The AMO's SSTA pattern was derived through regressing North Atlantic SST anomalies onto the AMO index, utilizing observations spanning 1900–2018. A restoring time scale of 10 days was employed, and for each AMO-positive and AMO-negative experiment, five ensemble members were generated.

The climatological mean states and external factors like greenhouse gases, solar forcing, and aerosols were maintained at preindustrial levels. The experiment members were each simulated for 110 years, with the model's output analyzed for the final 80 years.

*h. Significance test*

The statistical significance of the results was assessed at 90% and 95% confidence levels. To determine the effective degree of freedom, an autocorrelation method was employed in the significance tests.

## 3. Contributions of the TP and SP dynamics to the formation of MY El Niños

A total of 18 SY and 19 MY El Niños were identified in the observations during the period 1854–2018 using the classification method described in section 2c (see Table 1). In the CESM1 preindustrial simulation, a total of 167 SY and 185 MY El Niños were identified during model years 400–2200. The relative percentages of SY and MY El Niños in the CESM1 (47.4% and 52.6%, respectively) are very similar to those in the observations (48.6% and 51.4%, respectively) (Fig. 1a). The sample sizes of SY and MY El Niños in the CESM1 were approximately 10 times larger than those in the observations, providing a robust dataset for these events that accurately reflects their relative frequencies in the real world.

Using the TP and SP indices, we analyzed the relative strengths of the TP and SP ENSO dynamics during the first five seasons of the SY and MY El Niños in the CESM1 simulation. Figure 1b displays the index difference composite for the two event groups. The results indicate that the TP ENSO dynamic is dominant during the developing summer (June$^0$–August$^0$) to the decaying spring of the SY El Niño, whereas the SP ENSO dynamic is dominant for the MY El Niño. These findings are consistent with Yu and Fang (2018), which suggests that the SP ENSO dynamic plays a more significant role than the TP ENSO dynamic in forming the MY El Niño events. It is encouraging to find that the CESM1 simulation reasonably reproduces the observed linkages between the TP and SP ENSO dynamics and the SY and MY El Niños, making it suitable for studying the underlying dynamics of the MY El Niño.

To investigate the reasons behind the different dynamic dominance, we compared the seasonal variations of composite SST and surface wind anomalies between the SY and MY El Niños in Fig. 2. The figure uncovers three primary differences between the two groups: 1) the SY El Niño exhibits a stronger peak winter (December$^0$–February$^1$) intensity of SSTAs compared to the MY El Niño (Figs. 2c,h,m); 2) the SY El Niño triggers a more robust positive phase of the IOD during the developing fall season (Figs. 2b,g,l) and a more potent IOB warming during the decaying spring (Figs. 2d,i,n); and 3) the MY El Niño induces stronger anomalous southwesterly (SW) trade winds over the northeast Pacific than the SY El Niño from the developing summer to decaying summer. As mentioned, the connection between El Niño and the Indian Ocean plays a crucial role in facilitating the shift from El Niño to La Niña conditions through the TP ENSO dynamic, resulting in the formation of SY events. This negative feedback should be weaker during the MY El Niño due to the weaker IOD and IOB it induced. On the other hand, the MY El Niño has a stronger ability than the SY El Niño to trigger the seasonal footprinting mechanism because of its stronger trade wind anomalies over the NE Pacific.

The contrast in the strength of the seasonal footprinting mechanism between the MY El Niño and SY El Niño is evident in their composite differences during the peak winter-to-decaying summer seasons (Figs. 2m,n). The difference highlights a distinct warm phase of the subtropical SST footprinting, characterized by positive SSTAs extending from the NE Pacific into the tropical central Pacific, overlaid with SW trade wind anomalies. The

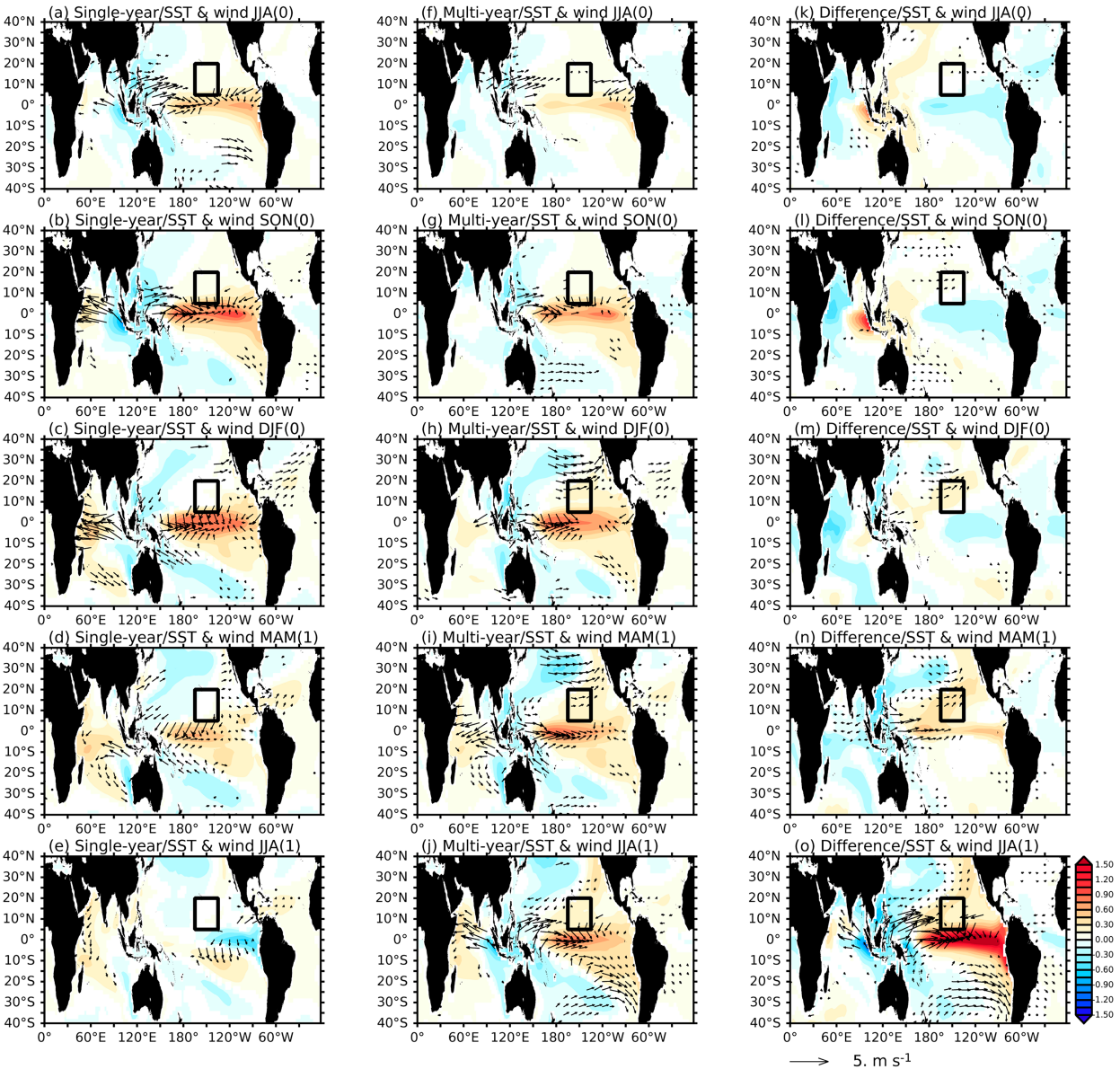


FIG. 2. Seasonal evolutions of SST (°C) and surface wind (m $s^{-1}$) anomalies composite for the (left) SY El Niño and (center) MY El Niño, and (right) their difference (MY El Niño minus SY El Niño). The seasonal evolutions shown from the top to bottom panels are the developing summer ($JJA^0$), fall ($SON^0$), peak winter ($D^0JF^1$), decaying spring ($MAM^1$), and summer ($JJA^1$). The color regions and black vectors indicate confidence levels exceeding 90% according to the Student's *t* test. The black box in all figures indicates the region where the trade wind index (165°–135°W, 5°–20°N) is defined.

warm SSTAs cause the El Niño to initiate a second El Niño from the tropical central Pacific in the $March^1$–$May^1$ ($MAM^1$) season.

The three distinguishing features explain why the MY El Niño has a stronger SP ENSO dynamic, while the SY El Niño has a more potent TP ENSO dynamic.

## 4. Key factors in activating the SP ENSO dynamics

The occurrence of trade wind anomalies over the NE Pacific is crucial for triggering the seasonal footprinting mechanism (Vimont et al. 2003) that forms the core of the SP ENSO dynamic. We next investigate why the NE Pacific experiences distinct trade wind anomalies during MY and SY El Niños, and whether the dissimilarity is linked to the properties of the events in the tropical Pacific and/or Indian Ocean. We defined a trade wind direction index (TWDI) to gauge the direction of trade wind anomalies in the subtropical Pacific (denoted by the black box in Fig. 2, where the largest trade wind differences between the MY and SY El Niños occur). Since the climatological NE trade has a wind direction of 225° (Fig. 3a), a small value of the TWDI (such as 0°–90°) indicates that the anomaly wind in the NE Pacific is in the opposite direction

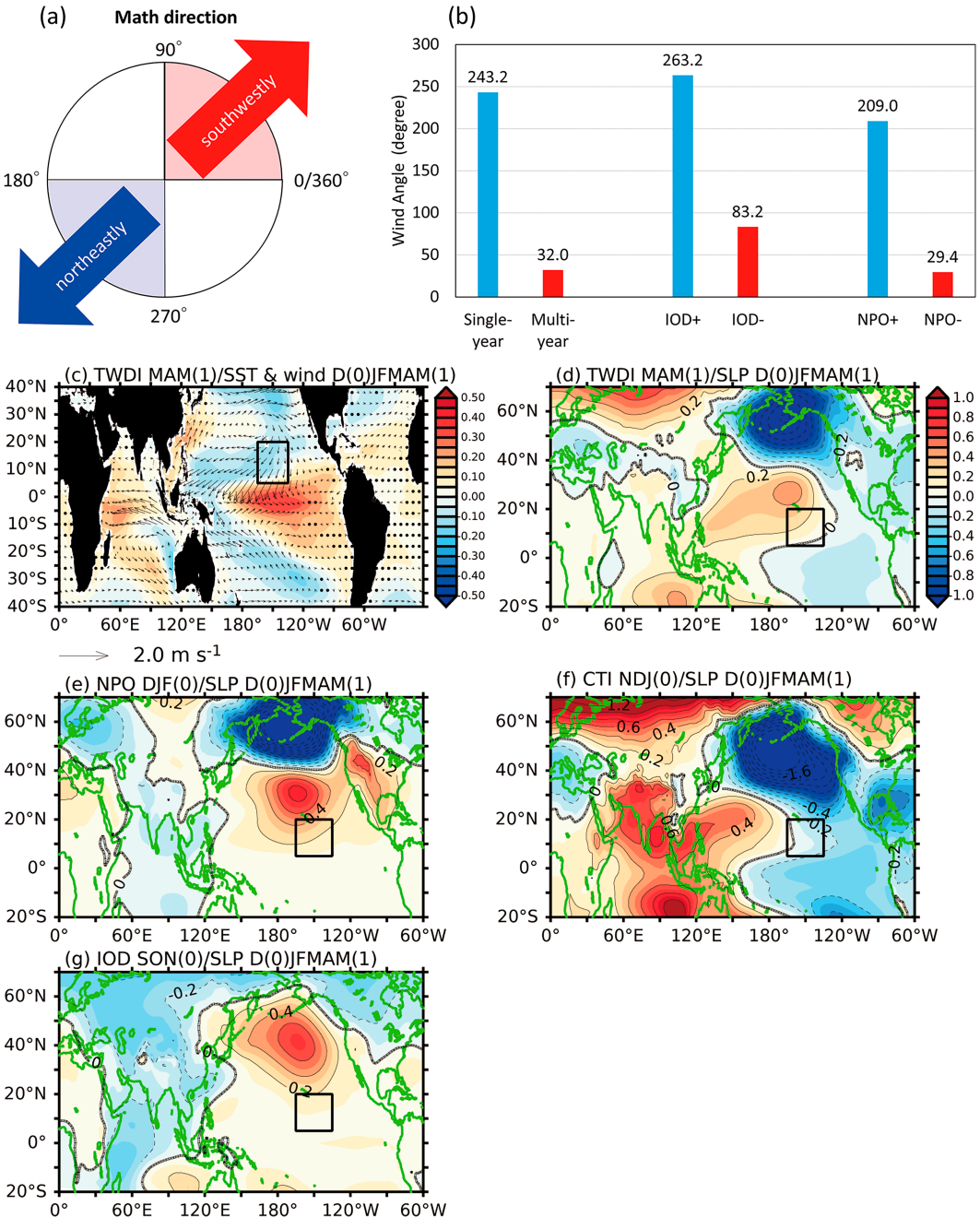


FIG. 3. (a) Schematic diagram illustrating how the mathematical direction of anomalous trade winds over the NE Pacific (i.e., the TWDI value) is determined and (b) its composite values during MY and SY El Niños and positive and negative IOD and NPO phases in the decaying spring period (March$^1$–May$^1$). (c) Lagged regressions of anomalous SST (shading; °C) and surface wind (vectors; m s$^{-1}$) during winter to spring (D$^0$JFMAM$^1$) onto the normalized trade wind direction index [TWDI, i.e., average anomalous wind direction in the black box in (c)] during decay spring (March$^1$–May$^1$). (d) As in (c), but for sea level pressure (SLP) (hPa). (e)–(g) Multiregression analysis of anomalous SLP during winter to spring (D$^0$JFMAM$^1$) onto peak winter (D$^0$JF$^1$) NPO, peak winter (ND$^0$J$^1$) CTI, and developing fall (SON$^0$) IOD indices. The black box in (c)–(g) indicates the region where the trade wind index (165°–135°W, 5°–20°N) is defined.

from the climatological trade and can reduce surface evaporation to trigger a warm phase of the seasonal footprinting mechanism. Conversely, a large value of TWDI indicates that the anomaly wind is aligned with the climatological trade and can trigger a cold phase of the seasonal footprinting mechanism. Figure 3b shows that the composite TWDI has a value of 243.2° during the SY El Niño but a value of 32.0° during the MY El Niño. These values suggest that the NE Pacific trade winds blow very much southwestward during the SY events but in an opposite direction during the MY events. This result confirms that the anomalous trade wind direction favors triggering a warm seasonal SST footprint in the MY El Niño but a cold SST footprint in the SY El Niño.

A lagged regression was conducted using the TWDI in $MAM^1$ to identify the primary patterns of SST anomalies in peak winter to decaying spring ($D^0JFMAM^1$; shown in Fig. 3c) that may lead to changes in the trade wind direction. The dominant SST anomalies identified in the regression were associated with El Niño and IOB warming conditions in the preceding winter and spring. An IOD-like characteristic is embedded in the Indian Ocean basin warming condition, with stronger warming in the western tropical Indian Ocean than in the eastern tropical Indian Ocean. As mentioned in section 1, the positive IOD typically induced by El Niño events during the developing $SON^0$ season later develops into a positive IOB pattern during El Niño's peak winter to early spring seasons. Therefore, the regression result indicates that the IOD phases during the developing fall season of El Niño play an important role in affecting trade wind anomalies over the subtropical Pacific. As large values of TWDIs are related to northeasterly winds, this regression provides insights into the SST conditions that can strengthen the climatological NE trades and trigger a cold SST footprint extending from the subtropical to tropical Pacific, which may transition a preceding El Niño condition into a La Niña condition, resulting in an SY El Niño event. Thus, the analysis suggests that for an El Niño event to persist into the second year and become an MY event, a weaker-intensity El Niño and/or a negative IOD phase during the first developing year of the El Niño is crucial. The impact of the IOD phase on the trade wind direction is further supported by the composite TWDI values during the positive and negative phases of the IOD (Fig. 3b). During the negative IOD phase, anomalous SW trades (with a composite TWDI of 83.2°) occur over the northeast Pacific, whereas during the positive phase, anomalous northeasterly trades (with a composite TWDI of 263.2°) are induced. It should be noted that we find CESM1 biases in simulating excessively strong and persistent IOD events compared to the observations (not shown). However, this bias does not lead to an overestimation of the importance of the IOD. A similar TWDI regression with SSTAs using the 1948–2018 observations (not shown) reveals a warm IOB condition similar to the one depicted in Fig. 3c, except that the IOD-like feature is weaker in the observations than in the CESM1 simulation. Nevertheless, the observed warm IOB is similarly preceded by a positive IOD in the previous $SON^0$ season.

A similar lagged regression with SLP anomalies (Fig. 3d) reveals that the northeasterly trade wind anomalies (i.e., large TWDI) are directly related to an anomalous high over the subtropical North Pacific. The regression also indicates that this anomalous high can be accompanied by an anomalous low over the North Pacific. Since this north–south dipolar SLP pattern resembles the spatial pattern of the NPO, the NPO can be a third factor (other than the El Niño intensity and IOD) in causing variations in trade wind direction. The composite TWDI values during the positive and negative phases of the NPO (Fig. 3b) confirm that the positive NPO can induce anomalous northeasterly trades (with large TWDI values) and the negative NPO can induce anomalous SW trades (with large TWDI values).

To determine the relative impacts of these three factors on TWDI-related SLP anomalies in the North Pacific, we conducted a multiple regression analysis. Specifically, we examined the relationships between winter-to-spring SLP anomalies and the CTI in the $ND^0J^1$ season, the IOD index in the $SON^0$ season, and the NPO index in the $D^0JF^1$ season. The results indicate that while the regression onto the NPO closely resembles the TWDI-regressed SLP anomaly pattern, the SLP regressions onto the CTI and IOD also produce SLP anomalies over the TWDI region, which can strengthen the NE Pacific trade winds. The regression with the NPO index (Fig. 3e) shows that the anomalous high in the southern lobe of the positive NPO induced anomalous northeasterly trades over the TWDI region. The regression with the CTI (Fig. 3f) indicates that an El Niño condition can stimulate a Gill-type response (Gill 1980), which forms a pair of Rossby waves straddling along the equatorial Pacific to the west. The positive SLP anomalies associated with the northern Rossby wave were located directly to the west of the TWDI region and contribute to the formation of anomalous northeasterly trades within the region. Finally, the regression with the IOD index (Fig. 3g) was characterized by large and positive SLP anomalies over the North Pacific. This anomalous high extends southward to produce anomalous northeasterly trade winds over the TWDI region. Previous studies have suggested that a positive IOD event can cause anomalous ascending over the western Indian Ocean, leading to the generation of a Rossby wave train. This wave train then propagates along the western Pacific rim, from Indo-China toward the North Pacific, which could potentially explain the appearance of the positive SLP anomalies over the North Pacific when regressed with the IOD (e.g., Annamalai et al. 2007; Shukla et al. 2009; Seo et al. 2016).

Our analyses above indicate that the positive and negative phases of the IOD and NPO can, respectively, activate the cold and warm SST footprint to favor the formation of SY and MY El Niño events. To further confirm these phase linkages, we analyzed the relative percentages of the numbers of SY and MY El Niño events during these two phases of the IOD and NPO in the observations and the CESM1 simulations (Fig. 4). Since the IOD typically peaks in the fall and the NPO peaks in winter, we used the developing fall ($SON^0$) value of the IOD index and the peak winter ($D^0JF^1$) value of the NPO index for the analysis. Figure 4 shows that more SY than MY El Niño events occurred during the positive IOD phase in both the observations and CESM1 simulation, whereas more MY than SY El Niño events occur during the negative IOD phase. This result confirms that the IOD plays a crucial role in determining the evolution pattern of El Niño, with the positive and negative IOD phases helping to form the SY and MY El Niño, respectively. The

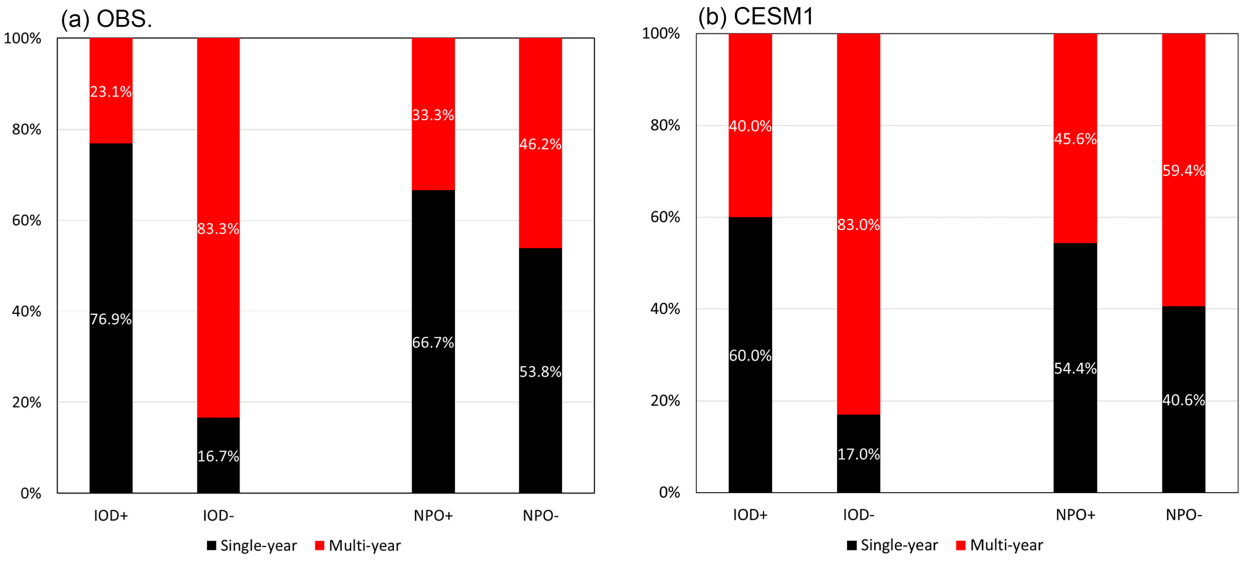


FIG. 4. The relative percentages of the numbers of single-year (black bars) and multiyear (red bars) El Niño events during IOD+, IOD−, NPO+, and NPO− phases. The percentages were calculated from (a) observations spanning 1948–2018 and (b) the preindustrial CESM1 model simulations covering years 400–2200. The developing fall ($SON^0$) value of the IOD index and the peak winter ($D^0JF^1$) value of the NPO index were used in the analysis.

analysis with the positive and negative phases of the NPO (Fig. 4) reveals that more SY than MY El Niño events occurred during the positive NPO phase and the reverse is true during the negative NPO phase in the CESM1 simulation. In the observations, although there are consistently more SY El Niño events than MY El Niño events in both the positive and negative NPO phases, the percentage of MY El Niño events increases from the positive to the negative NPO phase. Both the observations and the CESM1 simulation indicate that the negative phase of NPO encourages the occurrence of MY El Niño events. This influence is more pronounced in the CESM1 simulation than in the observations.

To further quantify the relative importance of IOD and NPO on influencing the occurrence percentages of SY and MY El Niño events, we utilize the following formula:

$$\Delta P = (|\mathrm{SYp} - \mathrm{MYp}| + |\mathrm{SYn} - \mathrm{MYn}|)/2.$$

Here, SYp and MYp represent the percentages of the numbers of SY and MY El Niño events that occurred during the positive phase of the factor examined, respectively. SYn and MYn represent the percentages that were observed during the negative phase of the factor, in the same manner. The $\Delta P$ index is used to measure the extent to which the phase of the factor can influence the relative dominance of the SY and MY patterns of El Niño. A larger $\Delta P$ value indicates that the factor has a more significant impact on differentiating the SY and MY evolution patterns for El Niño. Only the CESM1 simulation is used in the calculation (Fig. 5), and Table 2 illustrates the percentages of SY and MY events classified based on the phases of IOD and NPO in the simulation. As shown in Fig. 5, the $\Delta P$ values demonstrate that the IOD can cause a substantial difference in the relative percentages of SY and MY El Niño events, with an average difference of 43%. Meanwhile, the NPO results in a much smaller difference in the relative percentages, with an average difference of only 13.8%. This analysis confirms that the phase of IOD is a more critical factor than NPO in controlling the SY and MY evolution patterns of El Niño in the CESM1 simulation.

## 5. Intercorrelations among the three key factors

The three factors (i.e., El Niño intensity, IOD, and NPO) that can induce trade wind anomalies in the NE Pacific to trigger the SP ENSO dynamics are not necessarily independent from each other and may be intercorrelated. We show in Table 3 the

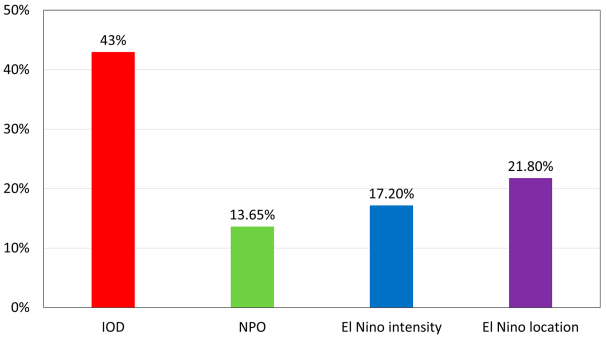


FIG. 5. The percentage differences ($\Delta P$) between the numbers of SY and MY El Niño events in the CESM1 preindustrial simulation related to the positive and negative phases of IOD and NPO, the strong and weak El Niño intensity (represented by the CTI index), and the central Pacific (CP) and eastern Pacific (EP) types of El Niño location (represented by the ZL Index). The $\Delta P$ is calculated based on the formula $\Delta P = (|\mathrm{SY}_p - \mathrm{MY}_p| + |\mathrm{SY}_n - \mathrm{MY}_n|)/2$. See text for the details of the formula.

TABLE 2. The percentage between the numbers of SY and MY El Niño events in the CESM1 preindustrial simulation related to the positive (Pos.) and negative (Neg.) phases of IOD and NPO, the strong and weak El Niño intensity (represented by the CTI index), and the central Pacific (CP) and eastern Pacific (EP) types of El Niño location (represented by the ZL index).

| | IOD ($SON^0$) | | NPO ($D^0JF^1$) | | CTI ($NDJ^0$) | | ZL ($NDJ^0$) | |
|---|---|---|---|---|---|---|---|---|
| SY/MY (%) | Pos. | Neg. | Pos. | Neg. | Strong | Weak | EP | CP |
| SY | 60.0% | 17.0% | 54.4% | 40.6% | 60.6% | 43.4% | 58.2% | 36.4% |
| MY | 40.0% | 83.0% | 45.6% | 59.4% | 39.4% | 56.6% | 41.8% | 63.6% |

correlations between the CTI index during $ND^0J^1$, the NPO index during $D^0JF^1$, and the IOD index during $SON^0$ in the CESM1 simulation. It shows that the IOD and CTI indices are highly correlated ($R = 0.56$, $p < 0.05$), indicating that a positive IOD phase typically occurs during a developing El Niño event. However, the NPO index has weak correlations with both the CTI ($R = 0.13$, $p < 0.1$) and IOD index ($R = -0.04$, $p > 0.1$), suggesting that NPO is mostly independent from these two major SST variability modes of the tropical Indo-Pacific Oceans. The NPO is mostly a free variability mode of the northern winter atmosphere (Rogers 1981), and its positive and negative phases can both occur during an El Niño event. The high correlation between El Niño and the IOD index means that an El Niño event and positive IOD it induced can work together to increase the chance of forming SY El Niño events through the SP ENSO dynamics (i.e., the stronger NE trade anomalies and a cold phase of the seasonal footprinting mechanism). This analysis infers that MY El Niño events are more likely to occur when the El Niño–IOD correlation is weak.

To decrease the positive correlation between El Niño and IOD and encourage the development of MY El Niño events, one possibility is to diminish the effectiveness of the atmospheric bridge mechanisms that generally connect El Niño events to positive IOD. These mechanisms are activated by the anomalous heating generated by El Niño events, which can disrupt the Walker circulation over the Indo-Pacific Oceans or initiate zonally propagating waves in the tropical troposphere, spreading the El Niño–induced warming to the adjacent Indian Ocean (Alexander et al. 2002; Cai et al. 2019; Chiang and Lintner 2005; He et al. 2020; Klein et al. 1999; Lau and Nath 2003; Su et al. 2005). The efficacy of these mechanisms may be influenced by the intensity and location of the El Niño SSTAs. We conducted a scattering plot analysis to examine the relationship between the IOD index and ENSO intensity (measured by the CTI index) and location (measured by the ZL index) for all El Niño events during their developing $SON^0$ season in both the observations and CESM1 simulation. As shown in Fig. 6, the IOD had a stronger positive correlation and regression slope with El Niño intensity than with El Niño location. This result suggests that El Niño intensity plays a larger role than El Niño location in affecting El Niño's ability to induce a positive IOD.

To further elucidate the impact of ENSO intensity and location on the relationship between El Niño and the IOD, we conducted a comparison of linear regressions of wind profiles along the equatorial Indo-Pacific sector onto ENSO intensity and location indices (Fig. 7). Figures 7a and 7b reveal two anomalous weaker Walker circulations over the Indo-Pacific region in the regression to the CTI index in both the observations and CESM1 simulation, which involve two strong ascending branches over the western Indian Ocean (around 60°E) and central Pacific (around 180°) and a descending branch over the western Pacific (around 120°E). The anomalous Walker circulation over the Indian Ocean has the ability to trigger a positive IOD. However, the anomalous Walker circulation over the Indian Ocean is not noteworthy in the regressions to the ZL index (Figs. 7c,d).

Our analyses indicate that the El Niño intensity is the main factor that determines how likely it is that a positive IOD can be induced by El Niño. When an El Niño is not strong enough, which based on Fig. 6 should be CTI < 0.71°C in the observations and 0.69°C in the CESM1 simulation, the typical El Niño–induced positive IOD may not occur. When the El Niño influence on IOD is weak, a negative IOD may occur during an El Niño event to activate a warm phase of the seasonal footprinting mechanism and increase the probability of forming MY El Niño events.

El Niño intensity and location also affect El Niño's ability to activate the seasonal footprinting mechanism via NE Pacific trade wind variations. To evaluate how the two properties of El Niño influence the percentage of SY and MY El Niño events, we categorized El Niño events into two groups based on ENSO intensity factor, namely, strong (CTI > 1 STD) and weak (CTI < 1 STD), and based on ENSO location factor, namely, EP type (ZL index > 0) and CP type (ZL index < 0). Then, we calculated the $\Delta P$ values accordingly. As shown in Fig. 5, the $\Delta P$ values are comparable based on either the ENSO intensity or ENSO location. Among all the factors we have considered in the $\Delta P$ analysis of Fig. 5, the phase of the IOD is still the most critical factor in controlling the occurrence of the SY or MY El Niño, followed by the El Niño properties (i.e., location and intensity), whereas the phase of the NPO was the least important factor.

TABLE 3. Correlations between the CTI index during $ND^0J^1$, IOD index during $SON^0$, and NPO index during $D^0JF^1$ in the CESM1 preindustrial simulation. The $p$ values of the correlations are shown in parentheses.

| $R/p$ value | Niño-3.4 | IOD | NPO |
|---|---|---|---|
| CTI | 1 | 0.56 ($p < 0.01$) | 0.13 ($p < 0.1$) |
| IOD | — | 1 | −0.04 ($p > 0.1$) |
| NPO | — | — | 1 |

## 6. AMO's impact on the El Niño–IOD relationship and MY El Niño occurrence

Our analyses above suggest that a strong El Niño–IOD relationship should favor the formation of SY El Niño events,

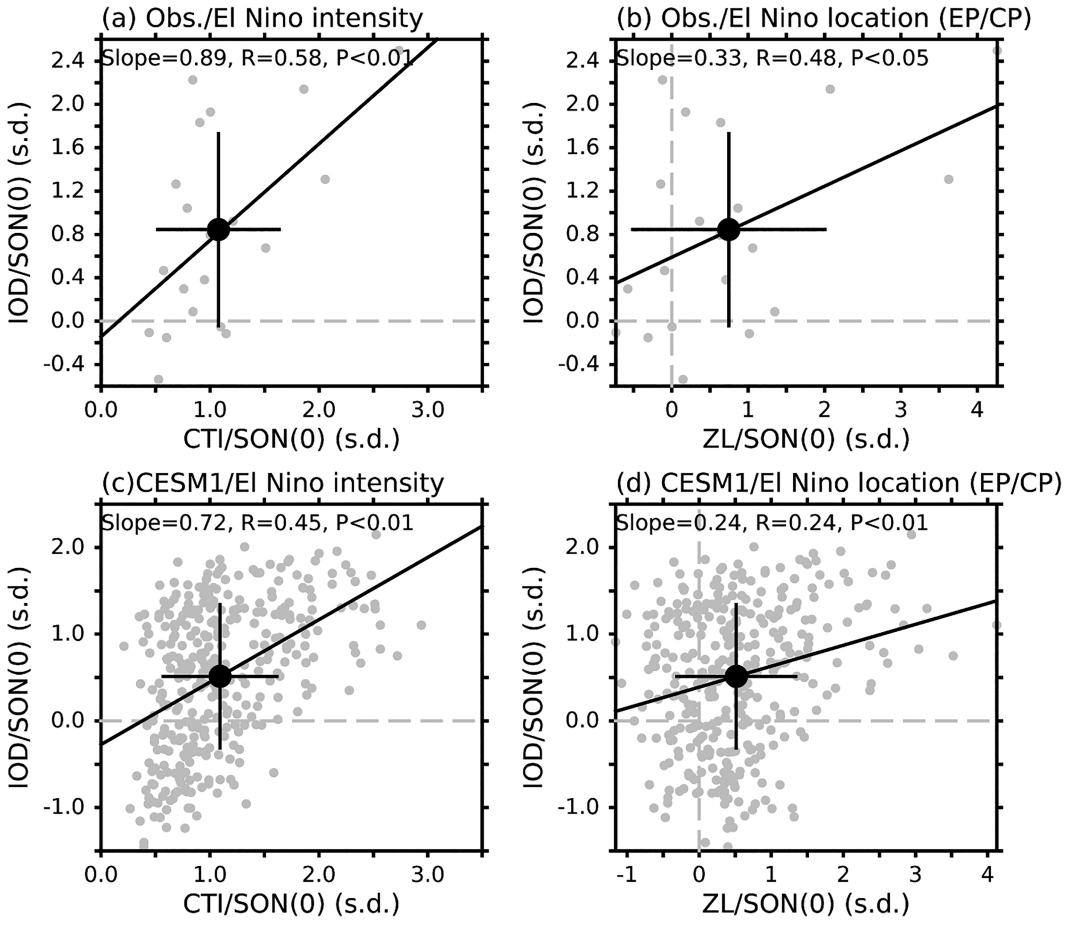


FIG. 6. Scattering plots depict (left) the relationship between the IOD index and the CTI index as well as (right) the zonal location (ZL) index during the developing fall ($SON^0$) of El Niño events. (a),(b) The observations from 1948 to 2018 and (c),(d) data from the CESM1 preindustrial simulation. In each panel, the mean value of all events is represented by a black dot and one standard deviation is indicated by vertical and horizontal lines centered on the dot. All indices were normalized.

while a weak relationship favors the formation of MY events through the SP ENSO dynamics. Other factors besides the intensity and location of El Niño events can also affect the El Niño–IOD relationship and thereby influence the frequencies of SY and MY El Niño events. One such factor is the AMO, which has been shown capable of impacting the mean climate state and variability of the Pacific, including ENSO (Ham et al. 2013; Wang et al. 2017; Yu et al. 2015). We examined the 21-yr running correlation between the developing fall ($SON^0$) Niño-3.4 and IOD indices in the observations from 1900 to 2018 (Fig. 8a) and found that the El Niño–IOD correlation is stronger during periods of negative AMO phases but weak during the periods of positive AMO phases. This suggests that when the AMO is in its positive phases, El Niño has a weaker influence on IOD, and vice versa for negative AMO phases. The antiphase relationship between AMO and IOD–Niño-3.4 correlations shown in Fig. 8a is statistically significant at the 95% interval (with a correlation of $-0.53$ and $p < 0.05$). Previous studies have indicated that a positive AMO phase can increase the strength of the SP ENSO dynamics (Yu et al. 2015) and give rise to more occurrences of the CP type of ENSO than the EP type. Since CP El Niño events are typically weaker than EP El Niño events (Kao and Yu 2009), the weaker and more CP-located El Niño is not conducive to triggering significant interactions between the Pacific Ocean and the Indian Ocean. Furthermore, a previous study (Wang and Wang 2014) has also revealed that CP El Niño events could trigger a negative IOD. These explain why the El Niño–IOD relationship is reduced during the positive AMO. The stronger SP ENSO dynamics and the weakened El Niño–IOD relationship together should favor the formation of MY El Niño events during positive AMO phases. Conversely, negative AMO phases should favor the occurrence of SY El Niño events. This effect is demonstrated in Fig. 8b, which illustrates that the relative percentage of the numbers of MY to SY El Niño events is higher during positive AMO phases (50%) than during negative AMO phases (37%).

To further examine the modulation of the AMO phase on the occurrence of MY El Niños, we conducted pacemaker experiments using a coupled AGCM-SOM model (see section 2f).

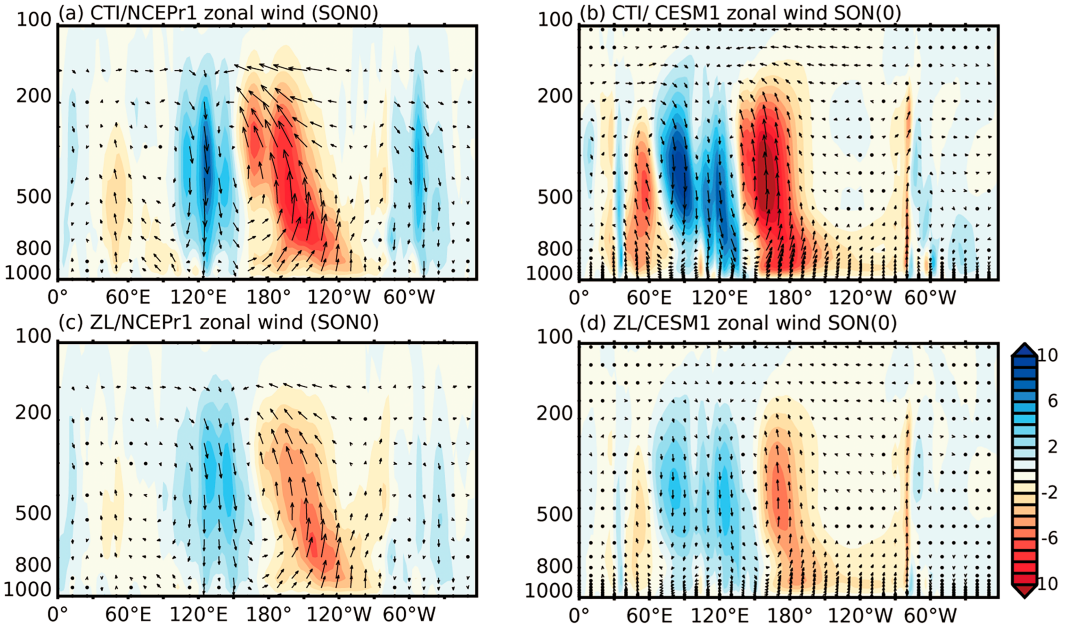


FIG. 7. Regressions of the anomalies in the equatorially averaged vertical velocities (colors; Pa $s^{-1}$) and zonal wind fields (vectors) onto the normalized (a) CTI and (c) ZL indices during the developing fall season ($SON^0$) in the observations. (b),(d) As in (a) and (c), respectively, but for the CESM1 preindustrial simulation. The vertical velocities displayed have been multiplied by −500.

Clement et al. (2011) demonstrated that a coupled AGCM–SOM model is capable of generating El Niños. However, it is important to note that this coupled model exclusively incorporates the SP ENSO dynamics, which rely on interactions between the atmosphere and the mixed-layer ocean, while excluding the TP ENSO dynamics, which involve thermocline variation and ocean circulation. Given that in this study we emphasize the pivotal role of SP ENSO dynamics in the occurrence of MY El Niño events, this AGCM–SOM model offers a simplified framework for exploring how modifications in the ENSO–IOD relationship can impact SP ENSO dynamics and subsequently influence the prevalence of MY El Niños. It is

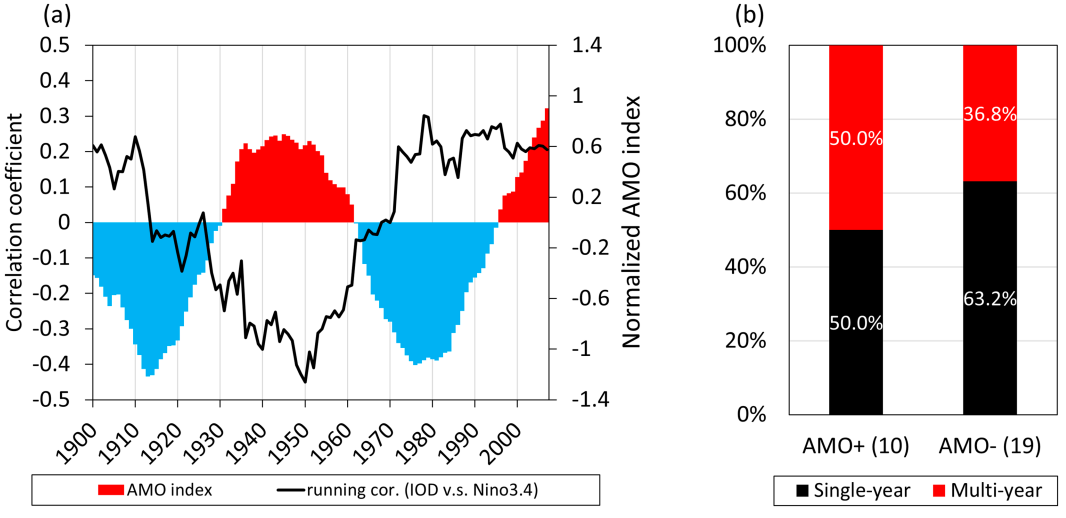


FIG. 8. (a) The time series of the normalized yearly AMO index after a 21-yr running mean (represented by the red and blue bars), and the 21-yr running correlation between the developing fall ($SON^0$) IOD and Niño-3.4 indices (shown by the black line; the value was removed from its mean of 0.45). (b) The bar graph displays the relative percentages (%) of SY (black) and MY (red) El Niño events during AMO positive and negative periods in observations from 1900 to 2018. Numbers in parentheses represent the total number of El Niño events during each period.

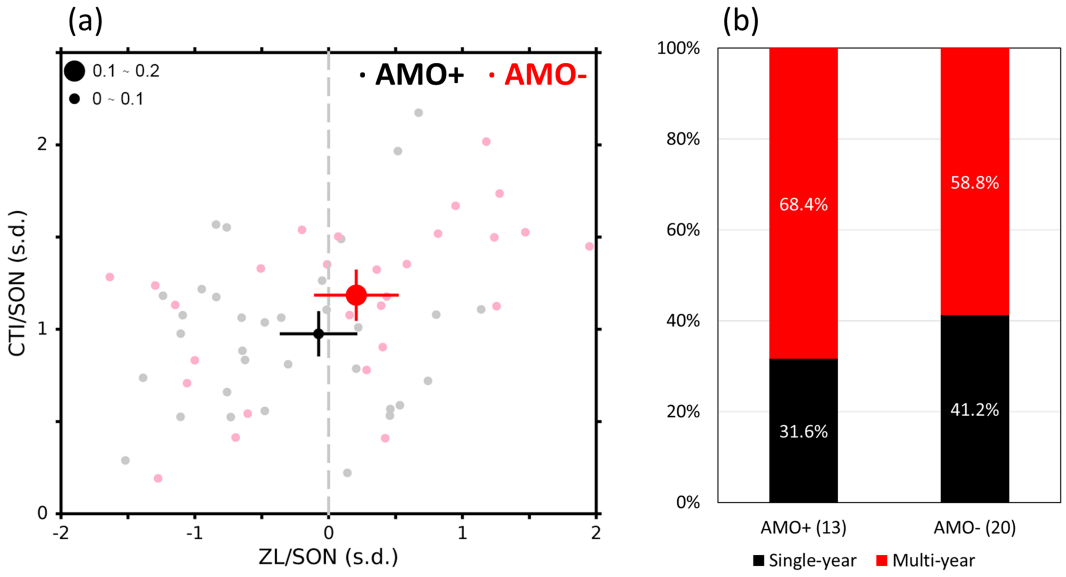


FIG. 9. (a) The values of the CTI and ZL indices during the developing fall ($SON^0$) of the El Niño events simulated in the AMO-positive (light gray dots) and AMO-negative (light pink dots) experiments are shown. The mean ZL and CTI index values in the former (dark black dot) and latter (dark red dot) experiments are also displayed, with their 90% confidence intervals indicated by the horizontal and vertical lines, respectively. The sizes of the dark red and black dots indicate the mean IOD values (STD units) during $SON^0$. (b) The relative percentages (%) of the numbers of SY (black bar) and MY (red bar) El Niño events during the AMO-positive and AMO-negative experiments. The numbers in parentheses indicate the total number of El Niño events identified in each of the experiments.

worth mentioning that ENSO-induced IOD events can arise due to atmospheric forcing triggered by ENSO, and as a result, these forced IOD events can occur even when ocean dynamics are not considered.

In the AMO-positive and AMO-negative experiments, we prescribed SSTAs of the positive and negative AMO phases, respectively, in the North Atlantic (0°–70°N). Meanwhile, the AGCM in other ocean basins was allowed to interact with the slab ocean. The CTI and ZL indices' mean values for the simulated El Niño events (see Fig. 9a) indicate that the AMO-positive experiment produced weaker and more CP-type El Niños, while the AMO-negative experiment produced stronger and more EP-type El Niños, consistent with the findings of Kao and Yu (2009) and Yu et al. (2015).

The IOD index during the simulated El Niños had a small mean value of 0.08 in the AMO-positive experiment and a positive value of 0.16 in the AMO-negative experiment (represented by dot size in Fig. 9a). This suggests that El Niño events have a stronger tendency to induce a positive IOD in the AMO-negative experiment than in the AMO-positive experiment, which aligns with our earlier analyses. Moreover, the correlation between the Niño-3.4 and IOD indices confirmed that the El Niño–IOD relationship was weaker in the AMO-positive experiment ($R = 0.02$, $p > 0.1$) than in the AMO-negative experiment ($R = 0.3$, $p < 0.01$). The relative percentages of the numbers of SY and MY El Niño events in the two experiments (Fig. 9b) showed that MY El Niño events occurred more frequently in the AMO-positive experiment (68.4%) than in the AMO-negative experiment (58.8%).

To delve deeper into the modulation effect of AMO on the El Niño–IOD relation under more realistic climatic conditions (specifically, by incorporating ocean dynamics), we conducted an additional set of pacemaker experiments. These experiments utilized the fully coupled model CESM1 (detailed in section 2h) and resulted in the generation of five ensemble members. In the AMO-positive and AMO-negative experiments, we nudged SSTAs of the positive and negative AMO phases, respectively, in the North Atlantic (0°–70°N). The mean values of the CTI index for the simulated El Niño events (Fig. 10a) indicate that the AMO-positive experiment produced weaker El Niños, whereas the AMO-negative experiment produced stronger ones. This result is consistent with the pacemaker experiences of AGCM-SOM (Fig. 9a). However, the ZL index yields a different result compared to the AGCM-SOM's pacemaker experiences. This disparity could potentially be attributed to the influence of ocean dynamics in the tropical region. Further investigation of this issue is warranted in future studies. In the context of the simulated El Niños, the IOD index displayed a modest and negative mean value of −0.28 in the AMO-positive experiment, while registering a positive value of 0.50 in the AMO-negative experiment (Fig. 10b). Additionally, examining the correlation between the Niño-3.4 and IOD indices affirmed that the El Niño–IOD relationship exhibited a reduced strength in the AMO-positive experiment ($R = 0.30$, $p < 0.1$) compared to the AMO-negative experiment ($R = 0.46$, $p < 0.05$) (Fig. 10c). Analyzing the relative percentages of SY and MY El Niño events in the two experiments (Fig. 10d) revealed a higher occurrence of MY El Niño events in the

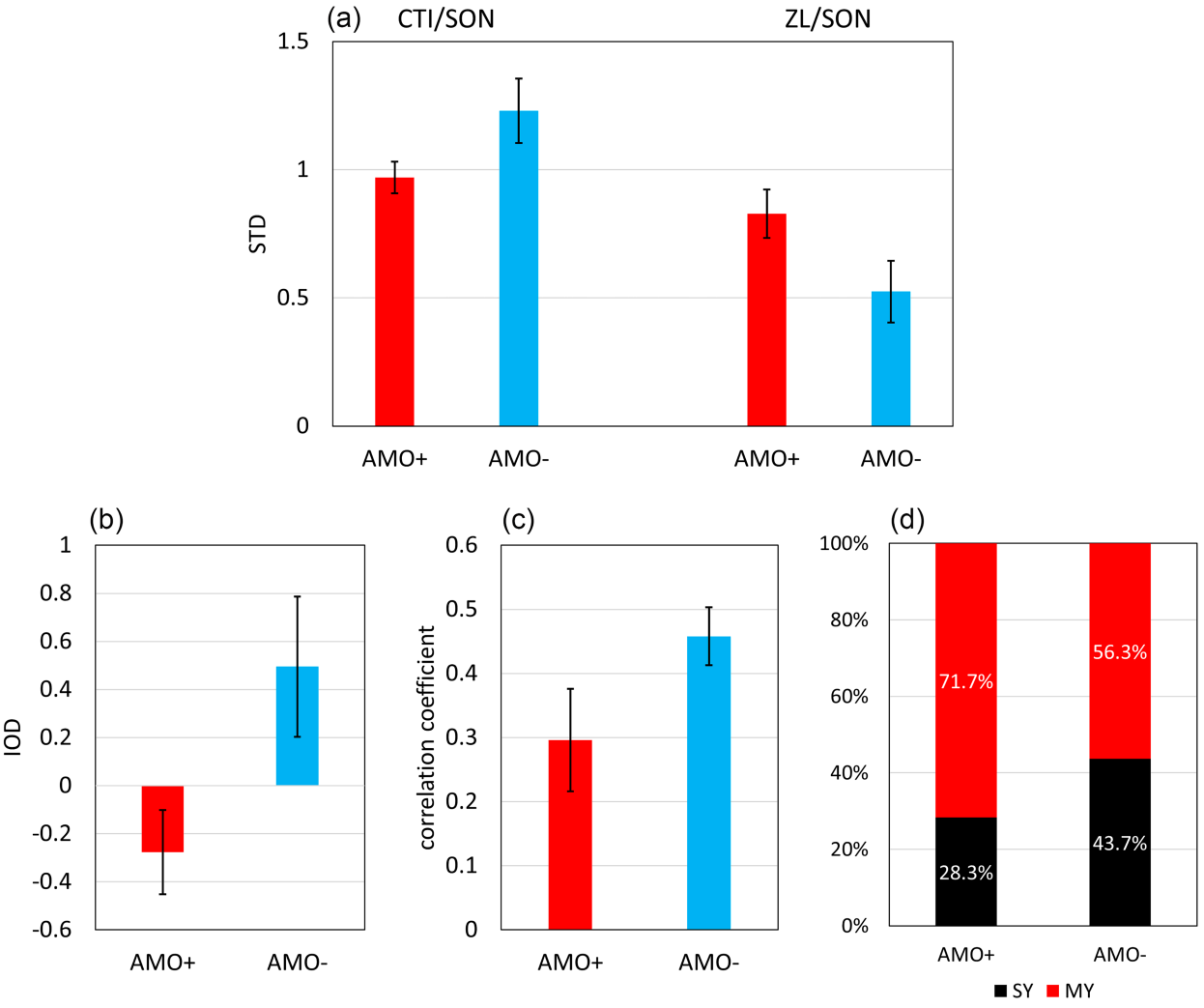


FIG. 10. (a) The ensemble mean of the CTI and ZL indices during the developing fall ($SON^0$) of the El Niño events simulated in the AMO-positive (red bars) and AMO-negative (blue bars) CESM1 pacemaker experiments. The error bars indicate their 90% confidence intervals. (b),(c) As in (a), but for the IOD index (STD) during the developing fall ($SON^0$) and the correlation between the developing fall Niño-3.4 and IOD indices, respectively. (d) The relative percentages of the numbers of SY (black bar) and MY (red bar) El Niño events during the AMO-positive and AMO-negative experiments. The numbers in parentheses indicate the total number of El Niño events identified in each of the experiments.

AMO-positive experiment (71.7%) in contrast to the AMO-negative experiment (56.3%). It is worth noting that the contrast in correlation between the Niño-3.4 and IOD indices in the AMO-positive and AMO-negative experiments appears to be less prominent when compared to the observed data (refer to Fig. 8). The underlying reasons for this divergence remain uncertain, but it may be attributed to potential deficiencies within the model's ability to accurately simulate ENSO, IOD, or other relevant processes. For instance, prior research (Jiang et al. 2021; Y.-S. Lin et al. 2023) has indicated that biases in ocean currents within the climate model could lead to a westward shift in the ENSO location, potentially affecting the model's representation of the ENSO–IOD relationship. More extensive investigations are needed to pinpoint the precise reasons for the differing ENSO–IOD relationships between model simulations and observations. Nevertheless, these inquiries fall outside the scope of our current study.

Overall, our two sets of pacemaker experiments lend support to the notion that MY El Niño events occur more frequently when the typical El Niño–positive IOD relationship weakens or breaks down, which is more likely to happen during the positive phase of the AMO. During the positive phase of the AMO, stronger easterly winds and the SP ENSO dynamics give rise to weaker and more CP-type El Niños (Kao and Yu 2009; Yu et al. 2015). These weaker El Niños are less likely to trigger the typical El Niño–induced positive IOD pattern (also referred to in Fig. 7), and the subsequent positive feedback mechanisms work to sustain the progression of the El Niño, leading to a more frequent occurrence of MY El Niños. In contrast, the negative phase of the AMO is characterized by a higher occurrence of

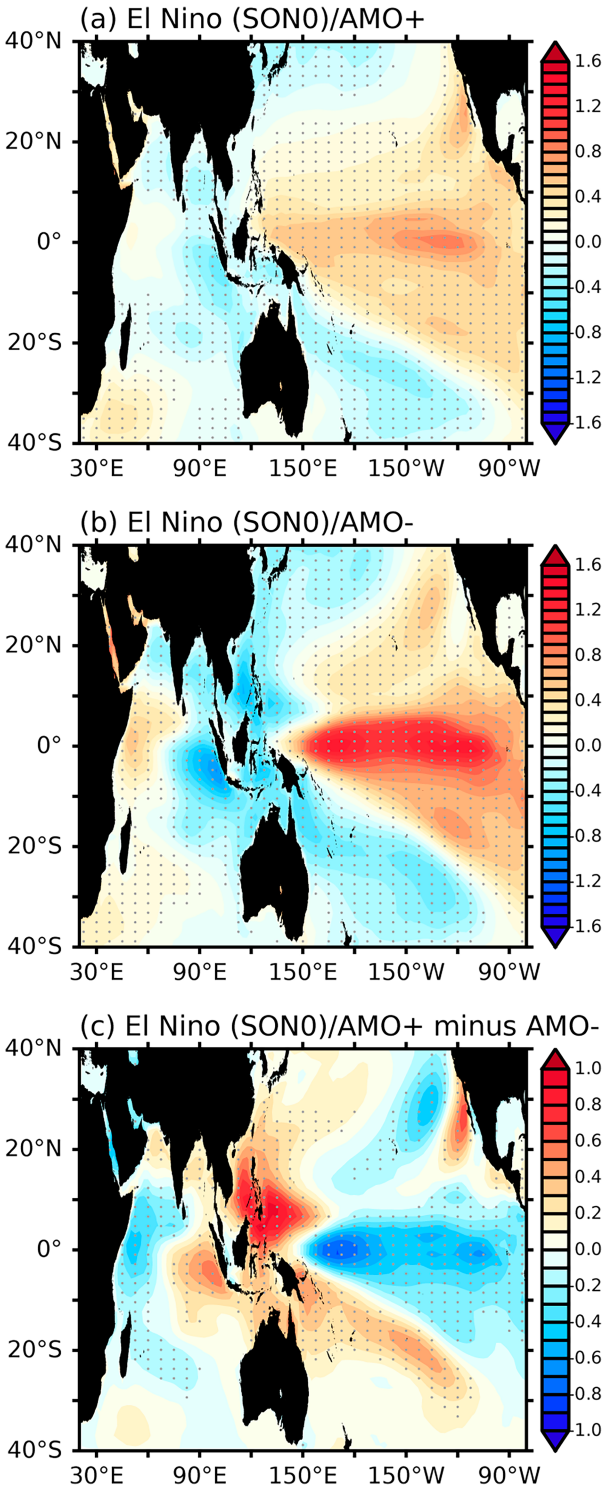


FIG. 11. The ensemble-mean SSTAs during the developing fall ($SON^0$) of the El Niño events simulated in the (a) AMO-positive and (b) AMO-negative pacemaker experiments with CESM1. (c) The difference between the AMO-positive and AMO-negative experiments. The stippled areas indicate confidence levels exceeding 95% according to the Student's *t* test.

stronger and more EP-type El Niños. This scenario is conducive to triggering the standard El Niño–induced positive IOD and the associated negative feedback, which collectively act to terminate the El Niño's development. Consequently, there is a more frequent prevalence of SY El Niños during this phase. We also examined the ensemble-mean SSTAs during the developing fall season ($SON^0$) of El Niño events simulated in both AMO-positive and AMO-negative experiments, along with their disparities (Fig. 11). The figures provide further support for our hypothesis. In the AMO-positive experiment (Fig. 11a), it becomes apparent that El Niño events exhibit reduced intensity compared to El Niño events simulated in the AMO-negative experiment (Fig. 11b). The heightened El Niño intensities produced in the AMO-negative experiment facilitate a more pronounced influence on the IOD, resulting in a robust ENSO–IOD relationship. Conversely, the attenuated El Niño intensities in the AMO-positive experiment diminish its ability to induce a positive IOD, consequently leading to a weaker ENSO–IOD relationship. These distinctions are notably conspicuous in Fig. 11c, which illustrates the differences in ensemble-mean SSTA between these two experiments.

Moreover, a study conducted by Zhang et al. (2022) proposes that SSTAs in the tropical Atlantic have the potential to influence the IOD through a series of interbasin interaction processes. The SSTAs in the Atlantic first trigger changes in atmospheric circulation, inducing either a cyclonic or anticyclonic pattern over the northwestern Pacific. These patterns subsequently bring about alterations in the Indo-Pacific Walker circulation, thereby impacting the variability of the IOD. Given that the AMO covers the North Atlantic region, the mechanism elucidated by Zhang et al. (2022) could serve as an additional explanation for how the AMO could modulate the El Niño–IOD relationship.

## 7. Conclusions

In this study, we have identified the IOD, NPO, and ENSO intensity and location as relevant factors that can activate the subtropical Pacific coupling processes behind the SP ENSO dynamic. Among them, the Indian Ocean is the most critical factor in determining whether a warm or cold phase of the SP ENSO dynamic is activated, resulting in SY or MY El Niño events. The ENSO intensity is crucial in determining if the typical El Niño–positive IOD relationship can emerge during an El Niño event. If it does, the induced positive IOD and the El Niño work together to activate the cold phase of the SP ENSO dynamic, resulting in an SY event. Otherwise, a neutral or negative IOD may activate the warm phase of the SP ENSO dynamic, leading to an MY event. We further conducted pacemaker coupled model experiments to show that the AMO can also affect the El Niño–IOD relationship, increasing the frequency of MY El Niño events during AMO-positive periods but decreasing it during AMO-negative periods.

Our study highlights the importance of considering not only the traditional TP ENSO dynamic but also the more recently developed SP ENSO dynamic, to understand the formation of MY El Niño events and the role of interbasin interactions in their formation. New insights are obtained in this study on the role of the Indian Ocean in ENSO evolution dynamics, which

can contribute to a better understanding of ENSO evolution dynamics and more accurate ENSO predictions.

*Acknowledgments.* We would also like to express our gratitude to Editor Yuko Okumura and three anonymous reviewers for their constructive comments, which have greatly contributed to the improvement of this paper. This research was supported by the Climate and Large-Scale Dynamics Program of the U.S. National Science Foundation under Grant AGS-2109539.

*Data availability statement.* The CESM1 simulation, which covers a period of 2200 years, was conducted by the CESM project team and is available via the Earth System Grid (https://www.earthsystemgrid.org/). The ERSST data used in the analysis were downloaded from the National Centers for Environmental Information/National Oceanic and Atmospheric Administration (https://www.ncei.noaa.gov/products/extended-reconstructed-sst), while the NCEP–NCAR Reanalysis 1 data were obtained from their website (https://www.esrl.noaa.gov/psd/data/gridded/data.ncep.reanalysis.html). The AMO index used in this study was obtained from http://www.esrl.noaa.gov/psd/data/timeseries/AMO/. The CESM1 pacemaker simulations data used in this study can be obtained by contacting Yong-Fu Lin at yongfulin0711@gmail.com.

## REFERENCES

Alexander, M. A., I. Bladé, M. Newman, J. R. Lanzante, N.-C. Lau, and J. D. Scott, 2002: The atmospheric bridge: The influence of ENSO teleconnections on air–sea interaction over the Global Oceans. *J. Climate*, **15**, 2205–2231, https://doi.org/10.1175/1520-0442(2002)015<2205:TABTIO>2.0.CO;2.

Anderson, B. T., 2004: Investigation of a large-scale mode of ocean–atmosphere variability and its relation to tropical Pacific sea surface temperature anomalies. *J. Climate*, **17**, 4089–4098, https://doi.org/10.1175/1520-0442(2004)017<4089:IOALMO>2.0.CO;2.

——, R. C. Perez, and A. Karspeck, 2013: Triggering of El Niño onset through trade wind–induced charging of the equatorial Pacific. *Geophys. Res. Lett.*, **40**, 1212–1216, https://doi.org/10.1002/grl.50200.

Annamalai, H., H. Okajima, and M. Watanabe, 2007: Possible impact of the Indian Ocean SST on the Northern Hemisphere circulation during El Niño. *J. Climate*, **20**, 3164–3189, https://doi.org/10.1175/JCLI4156.1.

Ashok, K., S. K. Behera, S. A. Rao, H. Weng, and T. Yamagata, 2007: El Niño Modoki and its possible teleconnection. *J. Geophys. Res.*, **112**, C11007, https://doi.org/10.1029/2006JC003798.

Battisti, D. S., and A. C. Hirst, 1989: Interannual variability in a tropical atmosphere–ocean model: Influence of the basic state, ocean geometry and nonlinearity. *J. Atmos. Sci.*, **46**, 1687–1712, https://doi.org/10.1175/1520-0469(1989)046<1687:IVIATA>2.0.CO;2.

Cai, W., and Coauthors, 2019: Pantropical climate interactions. *Science*, **363**, eaav4236, https://doi.org/10.1126/science.aav4236.

Capotondi, A., and Coauthors, 2015: Understanding ENSO diversity. *Bull. Amer. Meteor. Soc.*, **96**, 921–938, https://doi.org/10.1175/BAMS-D-13-00117.1.

Chang, P., L. Ji, H. Li, and M. Flügel, 1996: Chaotic dynamics versus stochastic processes in El Niño-Southern Oscillation in coupled ocean-atmosphere models. *Physica D*, **98**, 301–320, https://doi.org/10.1016/0167-2789(96)00116-9.

Chen, M., J.-Y. Yu, X. Wang, and W. Jiang, 2019: The changing impact mechanisms of a diverse El Niño on the western Pacific subtropical high. *Geophys. Res. Lett.*, **46**, 953–962, https://doi.org/10.1029/2018GL081131.

Chiang, J. C. H., and B. R. Lintner, 2005: Mechanisms of remote tropical surface warming during El Niño. *J. Climate*, **18**, 4130–4149, https://doi.org/10.1175/JCLI3529.1.

Chikamoto, Y., Z. F. Johnson, S.-Y. S. Wang, M. J. McPhaden, and T. Mochizuki, 2020: El Niño-Southern Oscillation evolution modulated by Atlantic forcing. *J. Geophys. Res. Oceans*, **125**, e2020JC016318, https://doi.org/10.1029/2020JC016318.

Clement, A., P. DiNezio, and C. Deser, 2011: Rethinking the ocean's role in the Southern Oscillation. *J. Climate*, **24**, 4056–4072, https://doi.org/10.1175/2011JCLI3973.1.

Deser, C., and J. M. Wallace, 1990: Large-scale atmospheric circulation features of warm and cold episodes in the tropical Pacific. *J. Climate*, **3**, 1254–1281, https://doi.org/10.1175/1520-0442(1990)003<1254:LSACFO>2.0.CO;2.

DiNezio, P. N., C. Deser, Y. Okumura, and A. Karspeck, 2017: Predictability of 2-year La Niña events in a coupled general circulation model. *Climate Dyn.*, **49**, 4237–4261, https://doi.org/10.1007/s00382-017-3575-3.

Enfield, D. B., A. M. Mestas-Nuñez, and P. J. Trimble, 2001: The Atlantic multidecadal oscillation and its relation to rainfall and river flows in the continental U.S. *Geophys. Res. Lett.*, **28**, 2077–2080, https://doi.org/10.1029/2000GL012745.

Fan, H., C. Wang, and S. Yang, 2023: Asymmetry between positive and negative phases of the Pacific meridional mode: A contributor to ENSO transition complexity. *Geophys. Res. Lett.*, **50**, e2023GL104000, https://doi.org/10.1029/2023GL104000.

Fang, S.-W., and J.-Y. Yu, 2020: Contrasting transition complexity between El Niño and La Niña: Observations and CMIP5/6 models. *Geophys. Res. Lett.*, **47**, e2020GL088926, https://doi.org/10.1029/2020GL088926.

Gill, A. E., 1980: Some simple solutions for heat-induced tropical circulation. *Quart. J. Roy. Meteor. Soc.*, **106**, 447–462, https://doi.org/10.1002/qj.49710644905.

Guan, C., X. Wang, and H. Yang, 2023: Understanding the development of the 2018/19 central Pacific El Niño. *Adv. Atmos. Sci.*, **40**, 177–185, https://doi.org/10.1007/s00376-022-1410-1.

Ham, Y.-G., J.-S. Kug, J.-Y. Park, and F.-F. Jin, 2013: Sea surface temperature in the north tropical Atlantic as a trigger for El Niño/Southern Oscillation events. *Nat. Geosci.*, **6**, 112–116, https://doi.org/10.1038/ngeo1686.

Hasan, N. A., Y. Chikamoto, and M. J. McPhaden, 2022: The influence of tropical basin interactions on the 2020–2022 double-dip La Niña. *Front. Climate*, **4**, 1001174, https://doi.org/10.3389/fclim.2022.1001174.

He, S., J.-Y. Yu, S. Yang, and S.-W. Fang, 2020: ENSO's impacts on the tropical Indian and Atlantic Oceans via tropical atmospheric processes: Observations versus CMIP5 simulations. *Climate Dyn.*, **54**, 4627–4640, https://doi.org/10.1007/s00382-020-05247-w.

Horii, T., and K. Hanawa, 2004: A relationship between timing of El Niño onset and subsequent evolution. *Geophys. Res. Lett.*, **31**, L06304, https://doi.org/10.1029/2003GL019239.

Huang, B., and Coauthors, 2017: Extended Reconstructed Sea Surface Temperature, version 5 (ERSSTv5): Upgrades, validations, and intercomparisons. *J. Climate*, **30**, 8179–8205, https://doi.org/10.1175/JCLI-D-16-0836.1.

Izumo, T., and Coauthors, 2010: Influence of the state of the Indian Ocean dipole on the following year's El Niño. *Nat. Geosci.*, **3**, 168–172, https://doi.org/10.1038/ngeo760.

Jiang, W., P. Huang, G. Huang, and J. Ying, 2021: Origins of the excessive westward extension of ENSO SST simulated in CMIP5 and CMIP6 models. *J. Climate*, **34**, 2839–2851, https://doi.org/10.1175/JCLI-D-20-0551.1.

Jin, F.-F., 1997: An equatorial ocean recharge paradigm for ENSO. Part II: A stripped-down coupled model. *J. Atmos. Sci.*, **54**, 830–847, https://doi.org/10.1175/1520-0469(1997)054<0830:AEORPF>2.0.CO;2.

Kalnay, E., and Coauthors, 1996: The NCEP/NCAR 40-Year Reanalysis Project. *Bull. Amer. Meteor. Soc.*, **77**, 437–471, https://doi.org/10.1175/1520-0477(1996)077<0437:TNYRP>2.0.CO;2.

Kao, H.-Y., and J.-Y. Yu, 2009: Contrasting eastern-Pacific and central-Pacific types of ENSO. *J. Climate*, **22**, 615–632, https://doi.org/10.1175/2008JCLI2309.1.

Kay, J. E., and Coauthors, 2015: The Community Earth System Model (CESM) large ensemble project: A community resource for studying climate change in the presence of internal climate variability. *Bull. Amer. Meteor. Soc.*, **96**, 1333–1349, https://doi.org/10.1175/BAMS-D-13-00255.1.

Kim, J.-W., and J.-Y. Yu, 2020: Understanding reintensified multiyear El Niño events. *Geophys. Res. Lett.*, **47**, e2020GL087644, https://doi.org/10.1029/2020GL087644.

——, and ——, 2021: Evolution of subtropical Pacific-onset El Niño: How its onset location controls its decay evolution. *Geophys. Res. Lett.*, **48**, e2020GL091345, https://doi.org/10.1029/2020GL091345.

——, and ——, 2022: Single- and multi-year ENSO events controlled by pantropical climate interactions. *npj Climate Atmos. Sci.*, **5**, 88, https://doi.org/10.1038/s41612-022-00305-y.

Klein, S. A., B. J. Soden, and N.-C. Lau, 1999: Remote sea surface temperature variations during ENSO: Evidence for a tropical atmospheric bridge. *J. Climate*, **12**, 917–932, https://doi.org/10.1175/1520-0442(1999)012<0917:RSSTVD>2.0.CO;2.

Kug, J.-S., and I.-S. Kang, 2006: Interactive feedback between ENSO and the Indian Ocean. *J. Climate*, **19**, 1784–1801, https://doi.org/10.1175/JCLI3660.1.

Lau, N.-C., and M. J. Nath, 2003: Atmosphere–ocean variations in the Indo-Pacific sector during ENSO episodes. *J. Climate*, **16**, 3–20, https://doi.org/10.1175/1520-0442(2003)016<0003:AOVITI>2.0.CO;2.

Lin, Y.-F., C.-T. Terng, C.-R. Wu, and J.-Y. Yu, 2023: Seasonally-reversed trends in the subtropical northwestern Pacific linked to asymmetric AMO influences. *Sci. Rep.*, **13**, 13735, https://doi.org/10.1038/s41598-023-40979-9.

Lin, Y.-S., L.-C. Wang, and J.-L. F. Li, 2023: Effects of equatorial ocean current bias on simulated El Niño pattern in CMIP6 models. *Geophys. Res. Lett.*, **50**, e2023GL102890, https://doi.org/10.1029/2023GL102890.

Lyu, K., J.-Y. Yu, and H. Paek, 2017: The influences of the Atlantic multidecadal oscillation on the mean strength of the North Pacific subtropical high during boreal winter. *J. Climate*, **30**, 411–426, https://doi.org/10.1175/JCLI-D-16-0525.1.

Okumura, Y. M., 2019: ENSO diversity from an atmospheric perspective. *Curr. Climate Change Rep.*, **5**, 245–257, https://doi.org/10.1007/s40641-019-00138-7.

——, M. Ohba, C. Deser, and H. Ueda, 2011: A proposed mechanism for the asymmetric duration of El Niño and La Niña. *J. Climate*, **24**, 3822–3829, https://doi.org/10.1175/2011JCLI3999.1.

Penland, C., and P. D. Sardeshmukh, 1995: The optimal growth of tropical sea surface temperature anomalies. *J. Climate*, **8**, 1999–2024, https://doi.org/10.1175/1520-0442(1995)008<1999:TOGOTS>2.0.CO;2.

Rogers, J. C., 1981: The North Pacific oscillation. *J. Climatol.*, **1**, 39–57, https://doi.org/10.1002/joc.3370010106.

Saji, N. H., B. N. Goswami, P. N. Vinayachandran, and T. Yamagata, 1999: A dipole mode in the tropical Indian Ocean. *Nature*, **401**, 360–363, https://doi.org/10.1038/43854.

Seo, K.-H., H.-J. Lee, and D. M. W. Frierson, 2016: Unraveling the teleconnection mechanisms that induce wintertime temperature anomalies over the Northern Hemisphere continents in response to the MJO. *J. Atmos. Sci.*, **73**, 3557–3571, https://doi.org/10.1175/JAS-D-16-0036.1.

Shukla, S. P., M. A. Chandler, J. Jonas, L. E. Sohl, K. Mankoff, and H. Dowsett, 2009: Impact of a permanent El Niño (El Padre) and Indian Ocean dipole in warm Pliocene climates. *Paleoceanography*, **24**, PA2221, https://doi.org/10.1029/2008PA001682.

Su, H., J. D. Neelin, and J. E. Meyerson, 2005: Mechanisms for lagged atmospheric response to ENSO SST forcing. *J. Climate*, **18**, 4195–4215, https://doi.org/10.1175/JCLI3514.1.

Suarez, M. J., and P. S. Schopf, 1988: A delayed action oscillator for ENSO. *J. Atmos. Sci.*, **45**, 3283–3287, https://doi.org/10.1175/1520-0469(1988)045<3283:ADAOFE>2.0.CO;2.

Vimont, D. J., J. M. Wallace, and D. S. Battisti, 2003: The seasonal footprinting mechanism in the Pacific: Implications for ENSO. *J. Climate*, **16**, 2668–2675, https://doi.org/10.1175/1520-0442(2003)016<2668:TSFMIT>2.0.CO;2.

Wang, C., and X. Wang, 2013: Classifying El Niño Modoki I and II by different impacts on rainfall in southern China and typhoon tracks. *J. Climate*, **26**, 1322–1338, https://doi.org/10.1175/JCLI-D-12-00107.1.

Wang, J.-Z., and C. Wang, 2021: Joint boost to super El Niño from the Indian and Atlantic Oceans. *J. Climate*, **34**, 4937–4954, https://doi.org/10.1175/JCLI-D-20-0710.1.

Wang, L., J.-Y. Yu, and H. Paek, 2017: Enhanced biennial variability in the Pacific due to Atlantic capacitor effect. *Nat. Commun.*, **8**, 14887, https://doi.org/10.1038/ncomms14887.

Wang, X., and C. Wang, 2014: Different impacts of various El Niño events on the Indian Ocean dipole. *Climate Dyn.*, **42**, 991–1005, https://doi.org/10.1007/s00382-013-1711-2.

——, W. Tan, and C. Wang, 2018: A new index for identifying different types of El Niño Modoki events. *Climate Dyn.*, **50**, 2753–2765, https://doi.org/10.1007/s00382-017-3769-8.

——, C. Guan, R. X. Huang, W. Tan, and L. Wang, 2019: The roles of tropical and subtropical wind stress anomalies in the El Niño Modoki onset. *Climate Dyn.*, **52**, 6585–6597, https://doi.org/10.1007/s00382-018-4534-3.

Wu, X., Y. M. Okumura, and P. N. DiNezio, 2019: What controls the duration of El Niño and La Niña events? *J. Climate*, **32**, 5941–5965, https://doi.org/10.1175/JCLI-D-18-0681.1.

——, ——, and ——, 2021: Predictability of El Niño duration based on the onset timing. *J. Climate*, **34**, 1351–1366, https://doi.org/10.1175/JCLI-D-19-0963.1.

Xie, S.-P., and S. G. H. Philander, 1994: A coupled ocean-atmosphere model of relevance to the ITCZ in the eastern Pacific. *Tellus*, **46A**, 340–350, https://doi.org/10.3402/tellusa.v46i4.15484.

Yu, J.-Y., and S.-W. Fang, 2018: The distinct contributions of the seasonal footprinting and charged-discharged mechanisms to ENSO complexity. *Geophys. Res. Lett.*, **45**, 6611–6618, https://doi.org/10.1029/2018GL077664.

——, H.-Y. Kao, and T. Lee, 2010: Subtropics-related interannual sea surface temperature variability in the central equatorial Pacific. *J. Climate*, **23**, 2869–2884, https://doi.org/10.1175/2010JCLI3171.1.

——, ——, ——, and S. T. Kim, 2011: Subsurface ocean temperature indices for central-Pacific and eastern-Pacific types of El Niño and La Niña events. *Theor. Appl. Climatol.*, **103**, 337–344, https://doi.org/10.1007/s00704-010-0307-6.

——, M.-M. Lu, and S. T. Kim, 2012: A change in the relationship between tropical central Pacific SST variability and the extratropical atmosphere around 1990. *Environ. Res. Lett.*, **7**, 034025, https://doi.org/10.1088/1748-9326/7/3/034025.

——, P.-K. Kao, H. Paek, H.-H. Hsu, C.-W. Hung, M.-M. Lu, and S.-I. An, 2015: Linking emergence of the central Pacific El Niño to the Atlantic multidecadal oscillation. *J. Climate*, **28**, 651–662, https://doi.org/10.1175/JCLI-D-14-00347.1.

——, X. Wang, S. Yang, H. Paek, and M. Chen, 2017: The changing El Niño–Southern Oscillation and associated climate extremes. *Climate Extremes: Patterns and Mechanisms*, *Geophys. Monogr.*, Vol. 226, Amer. Geophys. Union, 1–38, https://doi.org/10.1002/9781119068020.ch1.

Zhang, G., X. Wang, Q. Xie, J. Chen, and S. Chen, 2022: Strengthening impacts of spring sea surface temperature in the north tropical Atlantic on Indian Ocean dipole after the mid-1980s. *Climate Dyn.*, **59**, 185–200, https://doi.org/10.1007/s00382-021-06128-6.

Zheng, Y., W. Chen, S. Chen, S. Yao, and C. Cheng, 2021: Asymmetric impact of the boreal spring Pacific meridional mode on the following winter El Niño-Southern Oscillation. *Int. J. Climatol.*, **41**, 3523–3538, https://doi.org/10.1002/joc.7033.

Zhu, T., and J.-Y. Yu, 2022: A shifting tripolar pattern of Antarctic sea ice concentration anomalies during multi-year La Niña events. *Geophys. Res. Lett.*, **49**, e2022GL101217, https://doi.org/10.1029/2022GL101217.